Subcellular Comparison of Visible-Light Optical Coherence Tomography and Electron Microscopy in the Mouse Outer Retina

Pooja Chauhan,[1] Aaron M. Kho,[2] Paul FitzGerald,[3] Bradley Shibata,[4] and Vivek J. Srinivasan[1,2,5]

[1]Department of Radiology, NYU Langone Health, New York, New York, United States
[2]Department of Biomedical Engineering, University of California Davis, Davis, California, United States
[3]Department of Cell Biology and Human Anatomy, University of California Davis, Davis, California, United States
[4]Biological Electron Microscopy Facility, University of California Davis, Davis, California, United States
[5]Department of Ophthalmology, NYU Langone Health, New York, New York, United States

Correspondence: Vivek J. Srinivasan, Department of Radiology, NYU Langone Health, 550 1st Avenue, New York, NY 10016, USA; vivek.srinivasan@nyulangone.org.

Received: March 9, 2022
Accepted: June 30, 2022
Published: August 9, 2022

Citation: Chauhan P, Kho AM, FitzGerald P, Shibata B, Srinivasan VJ. Subcellular comparison of visible-light optical coherence tomography and electron microscopy in the mouse outer retina. *Invest Ophthalmol Vis Sci.* 2022;63(9):10. https://doi.org/10.1167/iovs.63.9.10

Purpose. We employed in vivo, 1.0-µm axial resolution visible-light optical coherence tomography (OCT) and ex vivo electron microscopy (EM) to investigate three subcellular features in the mouse outer retina: reflectivity oscillations inner to band 1 (study 1); hyperreflective band 2, attributed to the ellipsoid zone or inner segment/outer segment (IS/OS) junction (study 2); and the hyperreflective retinal pigment epithelium (RPE) within band 4 (study 3).

Methods. Pigmented (C57BL/6J, $n = 10$) and albino (BALB/cJ, $n = 3$) mice were imaged in vivo. Enucleated eyes were processed for light and electron microscopy. Using well-accepted reference surfaces, we compared micrometer-scale axial reflectivity of visible-light OCT with subcellular organization, as revealed by 9449 annotated EM organelles and features across four pigmented eyes.

Results. In study 1, outer nuclear layer reflectivity peaks coincided with valleys in heterochromatin clump density (-0.34 ± 2.27 µm limits of agreement [LoA]). In study 2, band 2 depth on OCT and IS/OS junction depth on EM agreed (-0.57 ± 0.76 µm LoA), with both having similar distributions. In study 3, RPE electron dense organelle distribution did not agree with reflectivity in C57BL/6J mice, with OCT measures of RPE thickness exceeding those of EM (2.09 ± 0.89 µm LoA). Finally, RPE thickness increased with age in pigmented mice (slope = 0.056 µm/mo; $P = 6.8 \times 10^{-7}$).

Conclusions. Visible-light OCT bands arise from subcellular organization, enabling new measurements in mice. Quantitative OCT–EM comparisons may be confounded by hydration level, particularly in the OS and RPE. Caution is warranted in generalizing results to other species.

Keywords: optical coherence tomography, electron microscopy, retinal pigment epithelium, retina, inner segment/outer segment junction

With the unique ability to distinguish disease processes in individual retinal layers, optical coherence tomography (OCT)[1,2] has become an ophthalmic standard of care in age-related macular degeneration (AMD),[3–7] diabetic retinopathy,[8,9] and glaucoma.[10,11] In OCT, each of the major layers of the retina gives rise to a distinct level of backscattering, or reflectivity.[2] This natural contrast mechanism has been critical to the success of OCT,[2] enabling segmentation algorithms[12] to quantify changes in disease.

With finer depth resolution and the averaging capabilities of high-speed OCT imaging techniques, bands that represent subcellular features are now visible, particularly in the outer retina.[13] These features are best exemplified in visible-light OCT, where numerous bands in the photoreceptors and retinal pigment epithelium (RPE)–Bruch's membrane (BM) complex have emerged.[14,15] As new bands appear, the question of their interpretation arises and controversies ensue.[16,17] Immunohistochemical markers may localize to a band,[18] but refractive index variations that give rise to backscattering and backreflection are most relevant for OCT.[19] Clinical relevance demands that we pinpoint the actual sources of OCT reflectivity.

Numerous animal studies have compared OCT against full-field light microscopy (LM) in the same subjects to assess or validate the ability of OCT to image[20] and measure[21–27] retinal layers. OCT has likewise been validated against confocal microscopy[28,29] and electron microscopy.[30,31] Yet, vigorous debate about the origins of some bands continues.[16,18,19,32] Most validation studies to date have used near-infrared OCT, with a depth resolution of 3.0 µm or coarser in vivo and as fine as 1.4 µm ex vivo, with LM,[20–26,33,34] with resolution limited by light diffraction.

Previously, in vivo visible-light OCT was validated against confocal microscopy,[29] yet only bands that are commonly visualized by near-infrared OCT were assessed. Although valuable, the limited definition of both the in vivo OCT and ex vivo validation images in these prior studies precluded a comparison of OCT reflectivity against subcellular organization and organelle distributions. Such an exacting comparison is needed to address ongoing debates.[35]

Electron microscopy (EM) provides a detailed accounting of organelles and other subcellular features[31,36] that create refractive index variations on a spatial scale that backscatter light. Here, we compare in vivo visible-light OCT, with 1.0-µm axial (depth) resolution, against ex vivo EM in the mouse outer retina. We compare OCT reflectivity and subcellular organization with respect to well-accepted reference surfaces. The micrometer-scale and organelle-level comparisons provide unique data to interpret ultrafine layers.

Study Rationales

Study 1. The outer nuclear layer (ONL) is a hyporeflective region containing the cell bodies of rods and cones. ONL thickness decreases in photoreceptor degeneration.[25,37] Recently, visible-light OCT revealed an ONL reflectivity pattern[14] that supposedly arose from laminar organization of nuclei, potentially providing a window into the ONL organization. To test this hypothesis, we compared OCT axial reflectivity against density of nuclear material.

Study 2. The integrity or intensity of band 2[38–47] has predicted visual outcome in numerous diseases such as macular hole repair,[44] cystoid macular edema,[46] acute zonal occult outer retinopathy,[47] retinitis pigmentosa,[43] dry and wet forms of AMD,[48] central serous chorioretinopathy,[49] polypoidal choroidal vasculopathy,[50] and uveitic macular edema.[51] Although there is no doubt about its clinical significance,[52] the origin of band 2 is the subject of considerable debate and controversy.[42] Initially attributed to the inner segment/outer segment (IS/OS) junction of the photoreceptors, with supporting biophysical evidence,[16] this band is now referred to as the ellipsoid zone (EZ).[17,53] Morphometry has been performed in the frog[54] and pig[31] to help resolve this debate. Some have hypothesized that adaptive optics (AO) OCT visualizes the IS/OS, and other non-AO OCT systems visualize the EZ.[42] Our non-AO visible-light OCT approach can help test this hypothesis. Also, a detailed comparison of OCT band 2 reflectivity with EM has not been performed in the rod-dominated mouse retina. Such a comparison is valuable, as resultant findings may apply to the peripheral human macula,[55] with some caveats.

Study 3. The functions of the RPE include protecting against light and free radicals, transporting nutrients, producing growth factors, regenerating visual pigments, and phagocytosing the OS, among others.[56] The RPE is a part of hyperreflective band 4,[57] with additional contributions from BM and, potentially, the rod OS tips or interdigitation zone. Directly assessing the health and composition of the RPE through non-invasive imaging would be highly significant,[36] yet reflectivity sources remain unclear.

Methods

OCT Imaging and Animal Preparation

The retinas of C57BL/6J ($n = 10$; eight males, two females; 11.8 ± 7.2 months old) and BALB/cJ ($n = 3$ males; 2 months old) mice from The Jackson Laboratory (Bar Harbor, ME, USA) were imaged in vivo with a free-space, visible-light, spectral-/Fourier-domain OCT system.[14] LM and EM were performed on a subset of the C57BL/6J mice (mouse number 1, 2.5 months old; mouse number 2, 4.5 months old; mouse number 3, 13 months old; mouse number 4, 19 months old). BALB/cJ mice were included to validate RPE thickness measurements and to confirm the impact of melanin on RPE bands. All studies were approved by the University of California, Davis, Institutional Animal Care and Use Committee. The study was conducted in accordance with the ARVO Statement for the Use of Animals in Ophthalmic and Vision Research, as well as National Institutes of Health and Animal Research: Reporting of In Vivo Experiments (ARRIVE) guidelines. The full spectral width of the spectrometer was 259 nm, and the axial resolution was 1.0 µm in tissue. The lateral resolution was 7.6 µm ($1/e^2$ intensity profile) with a depth of focus of 0.85 mm. Retinal imaging was performed with 300 µW power on the cornea and a 10 to 30 kHz line rate. Further details about imaging and reconstruction are described in Supplementary Note S1. Within a week of imaging, we euthanized mice by carbon dioxide inhalation and processed tissues for EM and LM, as described in Supplementary Note S2.

Comparison with LM

First, in vivo visible-light OCT was compared to LM of ex vivo histological slices (Fig. 1A). OCT contrast is based on transversally averaged reflectivity, and LM is based on dye absorption.[23] Therefore, visible-light OCT revealed several features that were not apparent histologically, and vice versa. In the inner retina, visible-light OCT showed sublaminar detail in many retinal bands, including a subtle decrease in reflectivity in S2 and S4 of the inner plexiform layer (Fig. 1B, lines), decreased reflectivity in the middle of the inner nuclear layer (Fig. 1C black bracket), and a thin region of moderate reflectivity between the hyperreflective outer plexiform layer and the hyporeflective ONL (Fig. 1C, gray bracket). These details are likely related to sublaminar organization of neurites or cell types,[58] some of which are appreciated in LM. In the outer retina, visible-light OCT depicted oscillations in reflectivity inner to the external limiting membrane (ELM), band 2, and the clear separation between the RPE and both the adjacent photoreceptor outer segment tips (OSTs) and BM (Fig. 1D). We investigated these features in studies 1, 2, and 3, respectively, as shown in Figure 1D. Because LM did not provide sufficient detail to validate these outer retinal bands, an EM approach was pursued.

Strategy for EM–OCT Comparison

Our intent in performing EM was to reveal subcellular organization that persist across the approximate lateral range for OCT averaging (~100 µm). Twenty adjacent A-line intensity profiles were extracted from each high-quality OCT image from each of three sampled locations. Then, multiple EM images were acquired across the sampled OCT locations and analyzed. Well-accepted reference surfaces were chosen to facilitate rigorous comparisons between modalities. Depending on the band of interest, a different reference surface was used. The selection criteria were a clear ELM and no blood vessel shadows. Profiles were corrected for the noise offset. The mean and standard deviation of the noise-corrected intensity were plotted for each location,

Investigative Ophthalmology & Visual Science

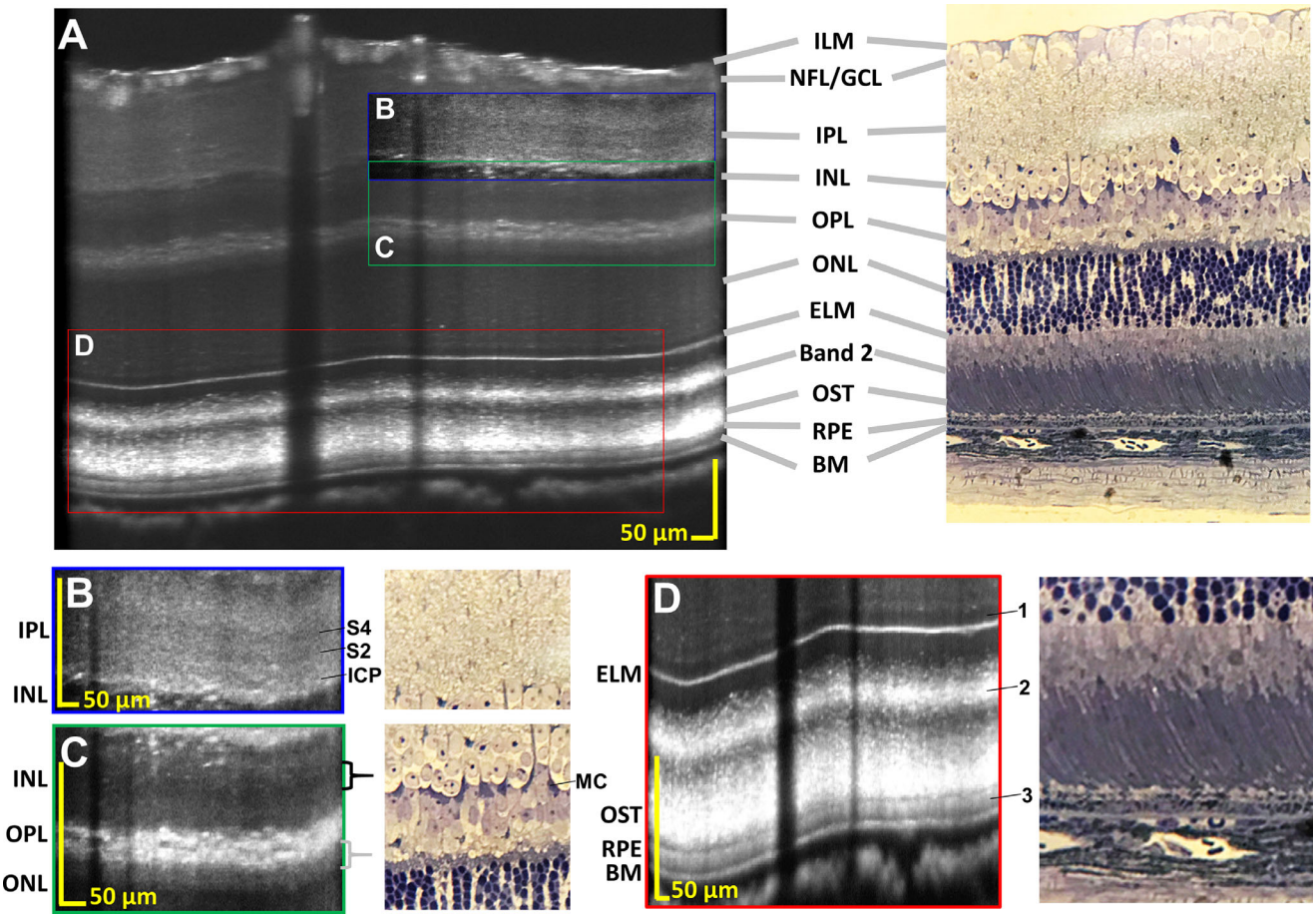

Figure 1. (**A**) Corresponding visible-light OCT image (*left*) and toluidine blue section (*right*) of the retina of mouse number 2. ILM, internal limiting membrane; NFL, nerve fiber layer; GCL, ganglion cell layer; IPL, inner plexiform layer; INL, inner nuclear layer; OPL, outer plexiform layer; ONL, outer nuclear layer; ELM, external limiting membrane; OST, photoreceptor outer segment tips; RPE, retinal pigment epithelium; BM, Bruch's membrane. The images were scaled vertically by aligning the ILM and BM. (**B–D**) Contrast-optimized and enlarged visible-light OCT images with approximate histological correlates (S2 is presumed IPL sublamina 2; S4 is presumed IPL sublamina 4). ICP, intermediate capillary plexus (excluding intersublaminar plexus); MC, Müller cell nucleus. The bands that are the subjects of studies 1 to 3 are marked in (**D**). Image scales are linear (**B**), square root (**C**), and logarithmic (**D**).

taking the reference surface as the origin. OCT image features (study 1, peak/valley intensity locations in ONL; study 2, band 2 depth; study 3, RPE thickness) were determined at each of the three locations, providing a mean and standard deviation for comparison against EM measurements of those same features.

Study 1

Anatomy. Nuclei in the ONL are visualized in EM as heterochromatin clumps (HCs). Rod nuclei possess one large heterochromatin clump, whereas cone nuclei exhibit multiple, irregularly shaped HCs.[59] Although the number of rod HCs should equal the number of rod nuclei, cone HCs should outnumber cone nuclei. We quantitatively compared OCT reflectivity with nuclear HC density.

Reference Surface. For this analysis, the reference surface was chosen to be the ELM, a well-accepted OCT hyperreflective band.[17,57] Anatomically, the ELM is a combination of homotypic (Müller cell to Müller cell) and heterotypic (Müller cell to photoreceptor) zonula adherens[60] that provides support to maintain metabolism, retinal anatomy, and homeostasis.[61] The ELM serves as a useful reference surface, as it is intrinsically very thin in the normal retina.[61] We analyzed 21 ± 11 EM images of the outer ONL and ELM per subject.

Study 2

Anatomy. The photoreceptor IS is divided into the myoid on the ELM side and the ellipsoid on the OS side.[17,57] The myoid zone has few mitochondria,[57,62] whereas the EZ is rich in mitochondria.[62] The high density of mitochondria, which scatter light in isolation, has led many to conclude that the EZ must be hyperreflective.[17,32] Here, we compared OCT reflectivity with the distribution of rod IS/OS junctions. A sufficiently large proximal shift of the reflectivity profile relative to the IS/OS distribution would support the EZ theory for band 2, but the absence of such a shift would weaken it.

Reference Surface. For this study, the ELM[17,57] was chosen as the reference surface. Importantly our image averaging protocol avoided ELM broadening (Fig. 1), which could otherwise lead to ambiguities in axial location that confound quantitative comparisons.[17] We analyzed 26 EM images of the IS and ELM per subject.

Investigative Ophthalmology & Visual Science

Study 3

Anatomy. The RPE cell contains a nucleus or nuclei, mitochondria, endoplasmic reticulum, Golgi, and electron-dense (ED) organelles such as pigmented melanosomes and melanolipofuscin.[63] Although it is generally acknowledged that melanosomes with melanin are a dominant source of RPE reflectivity,[36,64–68] the contributions of mitochondria and phagosomes have been debated.[61] As visible-light OCT now visualizes and quantifies multiple sub-bands within and around the RPE,[15,69] a thorough investigation of this band is warranted.

Reference Surface. For this study, the reference surface was chosen to be BM, also known as the vitreous lamina, as it is a well-accepted band in OCT.[17,57] BM plays a vital role in regulation and movement of biomolecules, nutrients, oxygen, and metabolic waste products to and from the retina. It serves as a useful reference surface, as its intrinsic thickness is expected to be on the order of 0.5 µm in mice.[55] BM also serves as the outer boundary for RPE thickness measurements. We analyzed 26 EM images of the RPE and BM per subject.

Results

Study 1

OCT images were flattened to the ELM (Figs. 2A, 2B). After flattening, ONL peaks and valleys were manually marked in each OCT line intensity plot (Fig. 2C). The ELM layer was delineated manually in EM images and fitted with a third-order polynomial (Figs. 2D, 2E). The positions of nuclear HCs in the ONL were manually marked, and distances were measured perpendicular to the ELM (Fig. 2E). Unfortunately, the ELM did not always align with the rectangular EM image field of view, meaning that, at some positions, the perpendicular to the ELM intersected the edge of the image within a few micrometers. To avoid the bias in nuclear HCs counts toward shorter ELM distances that such a misalignment would cause, we created a mask that included only regions of the ONL where a perpendicular distance (or depth) of up to 30 µm into the ONL from the ELM was measurable (Fig. 2E).

The depths (perpendicular distances) of masked ONL nuclear HCs relative to the ELM were quantified from EM. We initially did not distinguish rod and cone HCs (see Discussion for separate analysis of cone HCs). We marked a total of 3543 rod and cone nuclear HCs in the ONL across four animals. The counts were binned in 1-µm depth increments, and density was calculated by dividing the count number in a bin by the bin width of 1 µm and the ELM length in micrometers (Fig. 2F).

The line intensity plots (also known as longitudinal reflectivity profiles) revealed oscillations in intensity with distance away from the ELM, consistent with prior work.[14] Based on the previous supposition that ONL nuclear density could explain OCT reflectivity,[14] we convolved the EM distribution with an intensity (incoherent) point spread function and compared this profile to the actual OCT intensity profile (Fig. 2G). The width of the incoherent point spread function was estimated by fitting a Gaussian function of the OCT ELM intensity (Fig. 2C). The OCT peaks appeared to align with the valleys of the convolved EM density profile, suggesting that higher nuclear density correlated with lower reflectivity, contrary to our initial hypothesis.[14]

Having established that HC density peaks correspond to OCT intensity valleys, the depths of the following features relative to the ELM were compared: first peak EM–first valley OCT, first valley EM–first peak OCT, second peak EM–second valley OCT, and second valley EM–second peak OCT (Figs. 2H–2K). Overall, we found that OCT intensity peaks corresponded with valleys of the ONL HC density from EM, with –0.34 ± 2.27 µm limits of agreement (LoA) (Supplementary Fig. S1). This correspondence was consistent across all four mice with corresponding EM (Fig. 2, Supplementary Fig. S2).

Study 2

As in study 1, OCT images were flattened to the ELM (Figs. 3A, 3B). The ELM was delineated manually in the EM images and fitted with a third-order polynomial (Figs. 3C, 3D). The IS length, as revealed by EM, showed significant dispersion or variability between cells. The photoreceptor IS/OS junction positions were manually marked (Fig. 3D); distances were measured perpendicular to the ELM and denoted as IS/OS depth (Fig. 3E). To avoid the bias in IS/OS counts toward smaller depths (see study 1 for a detailed explanation), we created a mask that included only regions of the photoreceptors where a perpendicular distance (or depth) of up to 30 µm into the IS and OS from the ELM was measurable (Fig. 3D).

A potential problem in relating OCT and histologic measurements is that photoreceptor ISs may not be perpendicular to the ELM[70] and, thus, oblique to the OCT axis. In this situation, IS cell length may exceed IS/OS depth, defined as the perpendicular distance from the ELM. To guard against this, we verified that the IS axis was approximately perpendicular to the ELM and along the ONL cell columns. To guard against oblique slicing, we verified that measured ISs were continuous throughout the EM slice.

The depths (perpendicular distances) of masked rod IS/OS junctions relative to the ELM were quantified from EM. We marked a total of 1426 rod IS/OS junction depths across three animals. The counts were binned in 1-µm depth increments, and density was calculated by dividing the count number in a bin by the bin width and the ELM length in micrometers (Figs. 3E, 3F). We convolved the EM distribution with an intensity (incoherent) point spread function and compared this profile to the actual OCT intensity profile (Fig. 3G). The band 2[57] peak was also manually marked in each visible-light OCT line intensity plot, and the distance to the ELM was calculated, for eventual comparison with EM.

The convolved rod IS/OS density distribution (EM) and band 2 intensity (OCT) were similar across depth, except for the increased OCT reflectivity around the OS (Fig. 3G). The band 2 depth on OCT and IS/OS junction depth on EM agreed (–0.57 ± 0.76 µm LoA), with similar distributions (Figs. 3G, 3H). This correspondence was consistent across all three mice with corresponding EM (Fig. 3, Supplementary Fig. S3).

Study 3

OCT images were flattened to the outer retina (Figs. 4A, 4B). Note that BM is not fully flattened in Figure 4B, and profiles were selected from regions where BM was locally flat. BM was delineated manually in the EM images and fitted with a third-order polynomial (Figs. 4C, 4D). The positions of the ED organelles (melanosomes and melanolipofuscin)

Investigative Ophthalmology & Visual Science

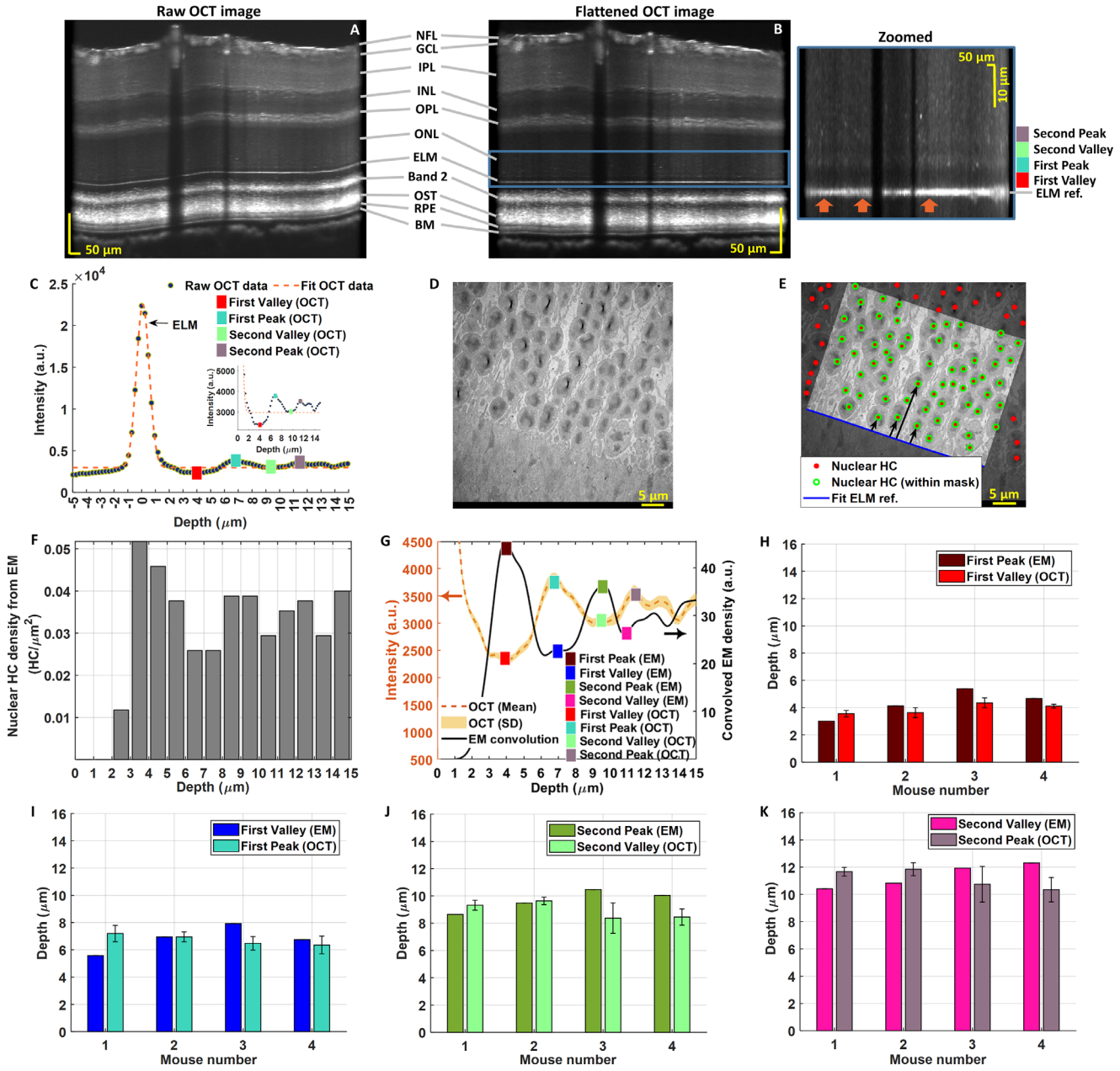

Figure 2. Visible-light OCT image of the retina of mouse number 2 before (**A**) and after (**B**) flattening with corresponding zoomed view of the outer ONL and ELM to visualize the dark band (*orange arrows* show locations of extracted line intensity plots). (**C**) OCT reflectivity profile with Gaussian fit. EM of nuclear HCs in the ONL cell layer are shown without (**D**) and with (**E**) the mask for data analysis (*black arrows* show positive depth). (**F**) Nuclear HC depth distribution from EM. Note that depth is positive in the proximal direction from the ELM. (**G**) OCT reflectivity and convolved EM density show an inverse relationship, with OCT intensity peaks corresponding with HC density valleys (see also Supplementary Fig. S2). (**H**) EM first peak and OCT first valley depths, (**I**) EM first valley and OCT first peak depths, (**J**) EM second peak and OCT second valley depths, and (**K**) EM second valley and OCT second peak depths as measured across four C57BL/6J mice. Error bars are standard deviations in OCT measurements across locations.

present in the RPE and apical processes were manually marked, and distances were measured perpendicular to BM (Fig. 4D). We did not distinguish among ED organelles, which included melanosomes, melanolipofuscin, and phagocytosed OSs, although the latter were rare.[28] The majority of ED organelles that we observed resembled melanosomes. To avoid biasing of organelle counts toward shorter BM distances (see study 1 for a detailed explanation), we created a mask that included only regions of the RPE and apical processes where a perpendicular distance (or depth) of up to 12 µm from BM was measurable. The RPE thickness was manually marked in each line intensity plot, determined as the distance from the BM peak to the RPE peak, for eventual comparison with EM (Fig. 4E).

The depths of 4480 RPE ED organelles relative to BM were quantified from EM across three pigmented animals. The counts were binned in 0.2-µm depth increments, and density was calculated by dividing the count number in a

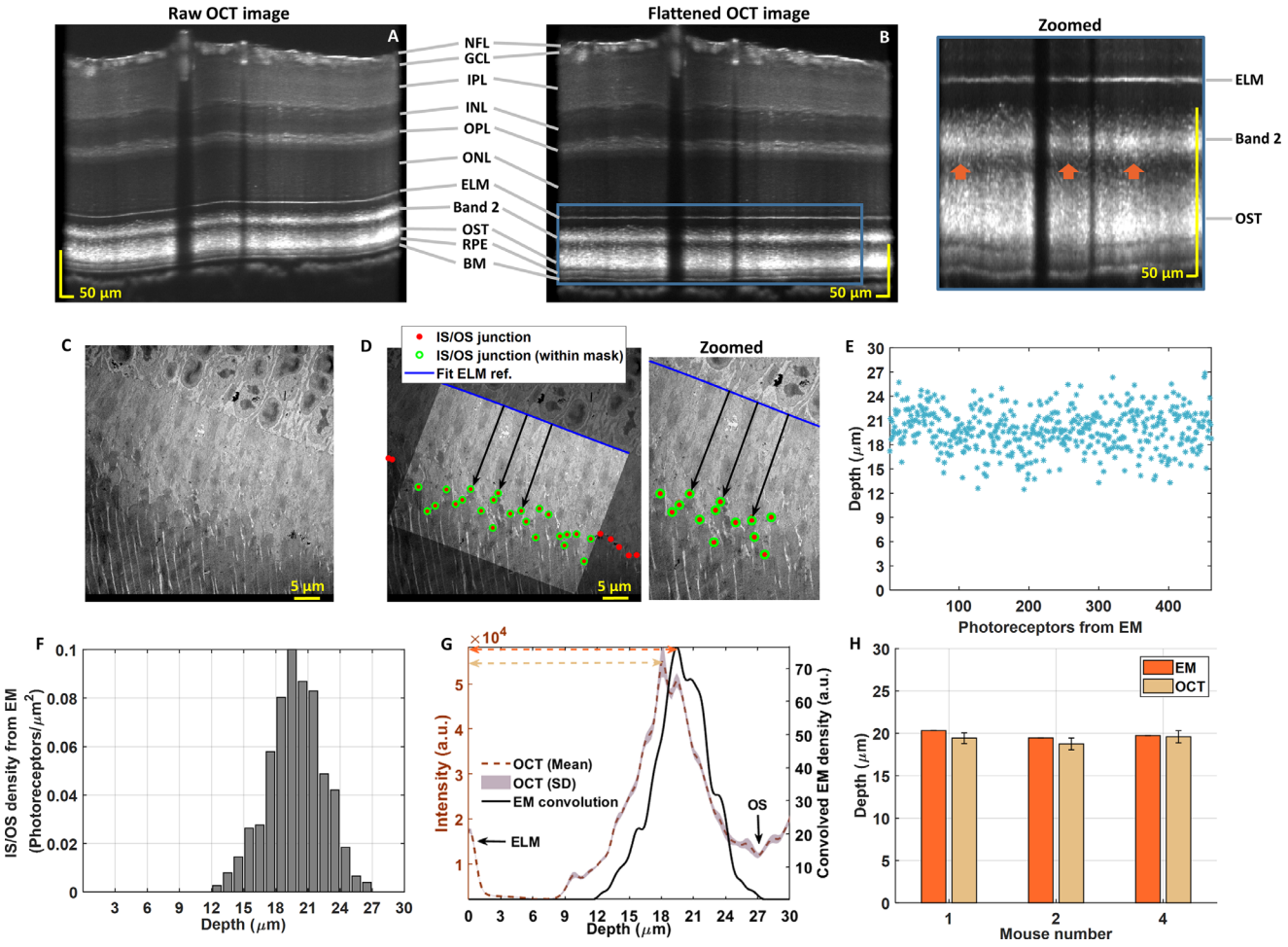

Figure 3. Visible-light OCT image of the retina of mouse number 2 before (**A**) and after (**B**) flattening with corresponding zoomed view of the ELM, IS/OS, and OST cell layers (*orange arrows* show locations of the extracted line intensity plots). EM of photoreceptor inner segments, shown without (**C**) and with (**D**) the mask for data analysis with corresponding zoomed view of IS/OS measurement (*black arrows* show positive depth). (**E**, **F**) IS/OS depth distribution relative to ELM (origin) from EM. Note that depth is positive in the distal direction from the ELM. (**G**) OCT reflectivity compared with convolved EM density profile (see also Supplementary Fig. S3). (**H**) IS/OS depth relative to the ELM, as measured by EM and OCT across three C57BL/6J mice. *Error bars* are standard deviations in OCT measurements across locations.

bin by the bin width and the BM length in micrometers (Fig. 4F). A bimodal profile with groups of ED organelles corresponding to both the RPE and apical processes was evident, even though the apical processes were not well preserved. We convolved the EM distribution with an intensity (incoherent) point spread function and compared this profile to the actual OCT intensity profile (Fig. 4G). The RPE thickness in EM was taken from BM (origin) to the first valley of the convolved profile, and the RPE thickness in OCT was taken from BM to either the RPE peak reflectivity (method 1) or the reflectivity minimum just outer to the OST (method 2) OCT. The RPE thickness on EM agreed moderately well with method 1 (0.38 ± 0.41 µm LoA) but not with method 2 (2.09 ± 0.89 µm LoA) (Fig. 4H). These trends were consistent across all three mice with corresponding EM (Fig. 4, Supplementary Fig. S4). Furthermore, albino mice were found to lack the RPE band of hyperreflectivity that was found in pigmented mice (Fig. 5). Finally, in our larger cohort of imaged pigmented mice, we detected a statistically significant thickening of the RPE with age (slope = 0.056 µm/mo; $P = 6.8 \times 10^{-7}$) (Fig. 6).

Discussion

This study presents a subcellular- and organelle-level comparison between visible-light OCT and EM in the pigmented mouse retina. ONL nuclear density, IS/OS junction location, and RPE organelle distribution were found to be precisely organized locally across multiple cells. This organization provides a mechanism for visible-light OCT to reveal subcellular organization with micrometer-scale axial, but not lateral, resolution.[71]

Study 1

Recently, a hyporeflective band inner to the ELM was reported by Kho et al.[14] in the mouse. This band was hypothesized to correspond to a cell nuclei free layer inner to the ELM.[14] The rigorous analysis here revealed that in fact the intensity in the ONL oscillates with diminishing amplitude farther from the ELM. These reflectivity oscillations were mirrored by nuclear HC density, with higher ONL intensity coinciding with lower nuclear HC density on EM. This find-

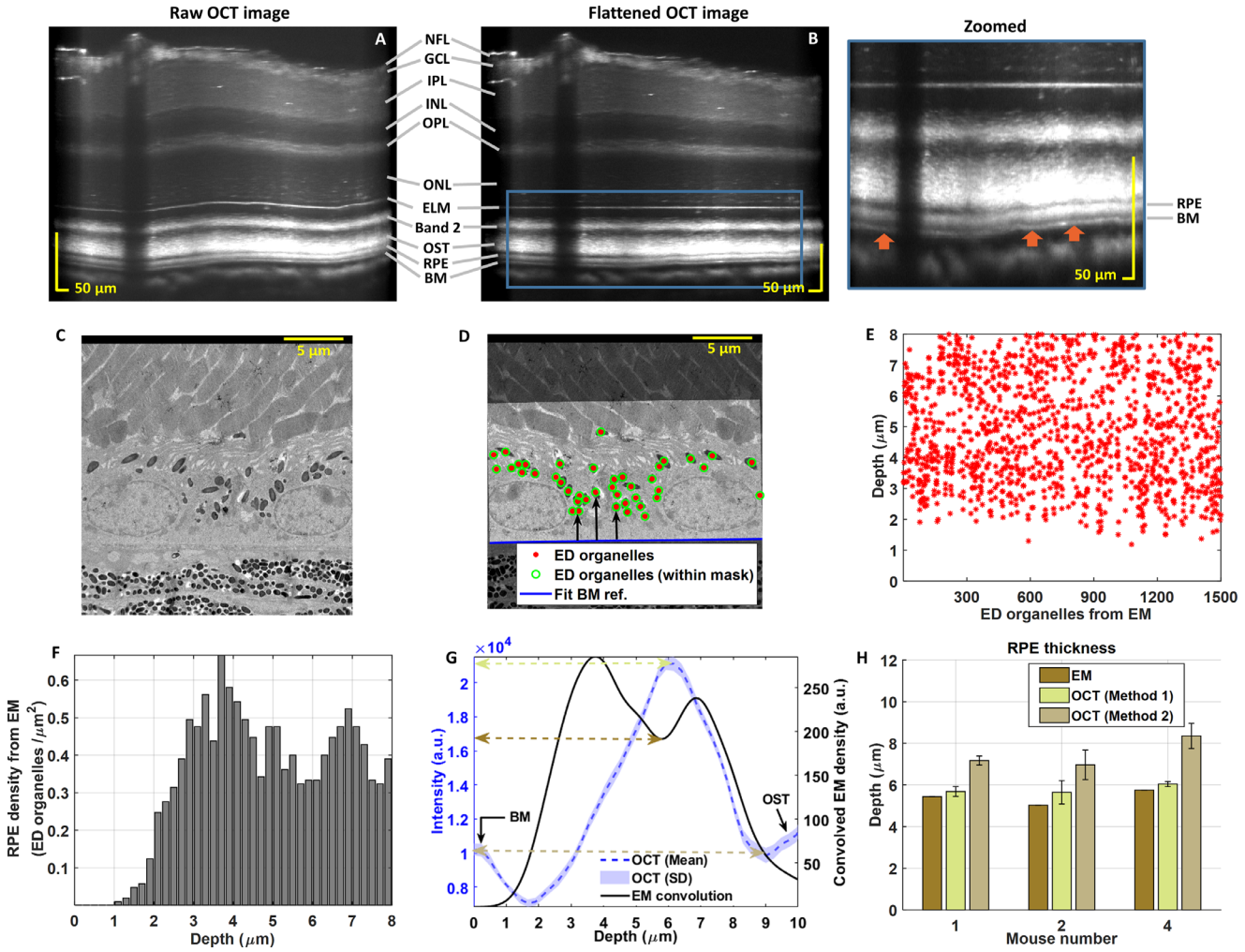

Figure 4. Visible-light OCT image of the retina of mouse number 4 before (**A**) and after (**B**) flattening with corresponding zoomed view of outer RPE and BM cell layers (*orange arrows* show locations of the extracted line intensity plots). EM of ED organelles in the RPE cell layer, shown without (**C**) and with (**D**) the mask for data analysis (*black arrows* show positive depth). (**E**, **F**) ED organelle depth distribution from EM. Note that depth is positive in the proximal direction from BM. (**G**) OCT reflectivity compared with convolved EM density profile (see also Supplementary Fig. S4). (**H**) RPE thickness by EM and OCT (see *dotted lines* in **G**), as measured by EM and OCT with methods 1 and 2 across three C57BL/6J mice. Method 1, BM peak to RPE peak reflectivity; method 2, manually drawn BM to the outer OST boundary. *Error bars* are standard deviations in OCT measurements across locations.

ing was contrary to our initial hypothesis[14] but consistent with the overall low reflectivity of nuclear layers on OCT.[2] The results suggest that local variations in nuclear density and the tendency of ONL nuclei to arrange in rows are responsible for band-like modulations of ONL reflectivity.

We also considered potential differences in rod and cone nuclear contributions to the ONL intensity oscillations. For example, a hyporeflective band inner to ELM, ostensibly similar to that reported by Kho et al.,[14] was attributed to cone nuclei in the porcine retina[31]; could such an explanation apply in the mouse retina? Although it is true that cone nuclei in the mouse retina also tend to localize adjacent to the ELM, cones account for just 3% of the photoreceptors in the mouse retina,[59] but cones account for one in four photoreceptors in the pig retina.[72] Nevertheless, for completeness, we investigated the distribution of cone nuclei independently (Supplementary Fig. S5). Cones accounted for just 8% of the nuclear HCs up to 30 µm from the ELM in the retina of mouse number 1 and were mainly concentrated 4 to 10 µm from the ELM (Supplementary Fig. S5). Thus, cone nuclei alone do not account for the reflectivity pattern in the outer ONL of the mouse retina.

Study 2

We aimed to add to the ongoing discussion on the band 2 origins[16,17] by comparing ultrahigh-resolution visible-light OCT of band 2 and EM localization of the rod IS/OS. The close correspondence between reflectivity and IS/OS depth distribution, relative to the ELM, suggests that outer retinal band 2 is predominantly explained by the IS/OS junction. How can an interface account for an OCT band that is more than 10 µm thick? Jonnal et al.[16] suggested that dispersion of cone IS length and IS/OS depth could thicken band 2 in humans, but they did not examine rods.[35] The present work

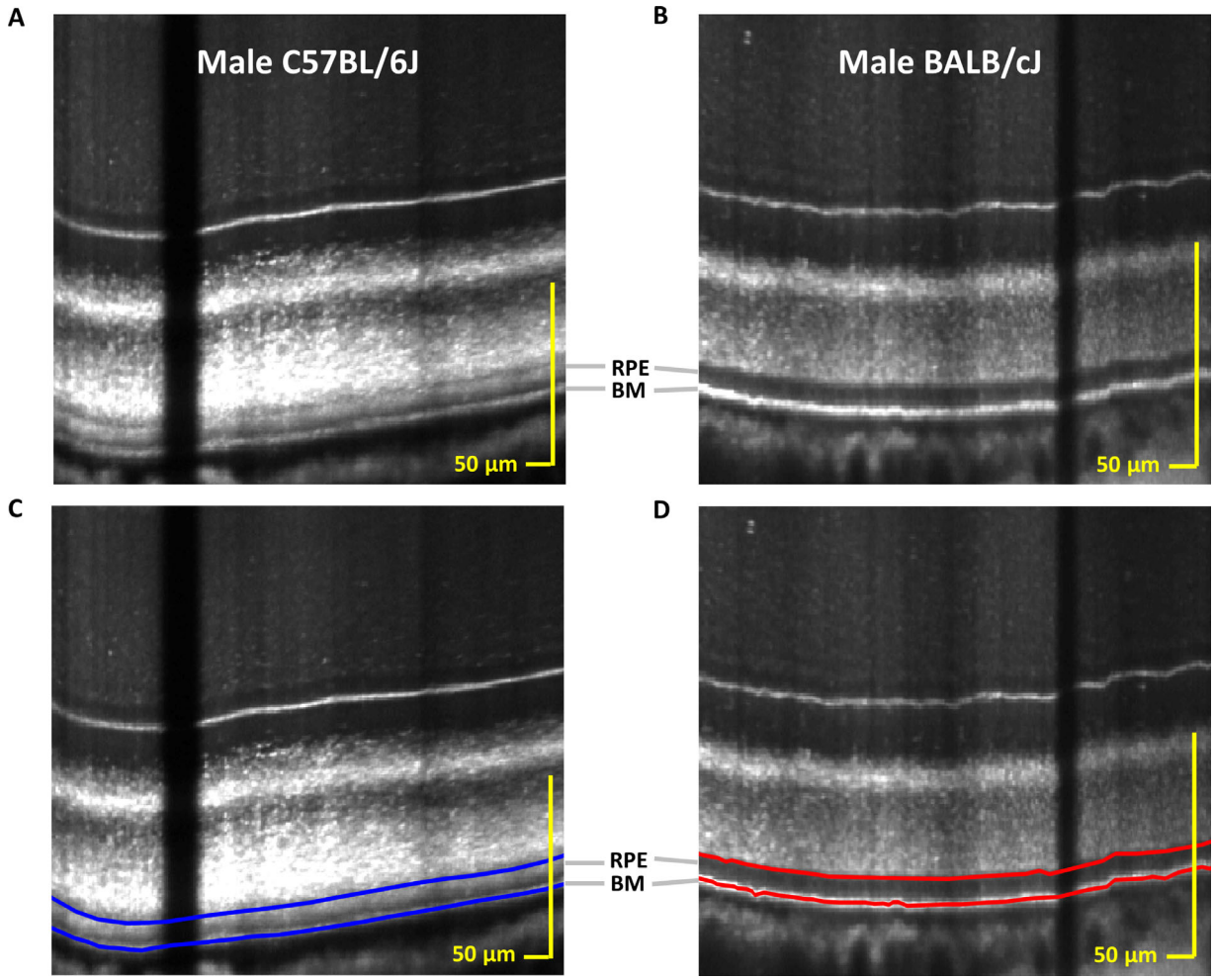

Figure 5. Visible-light OCT images of a young adult male C57BL/6J mouse retina without (**A**) and with (**C**) manual marking of RPE boundaries. Visible-light OCT image of a young adult male BALB/cJ mouse retina without (**B**) and with (**D**) manual marking of RPE boundaries (*blue lines* highlight the C57BL/6J RPE and *red lines* highlight the BALB/cJ RPE).

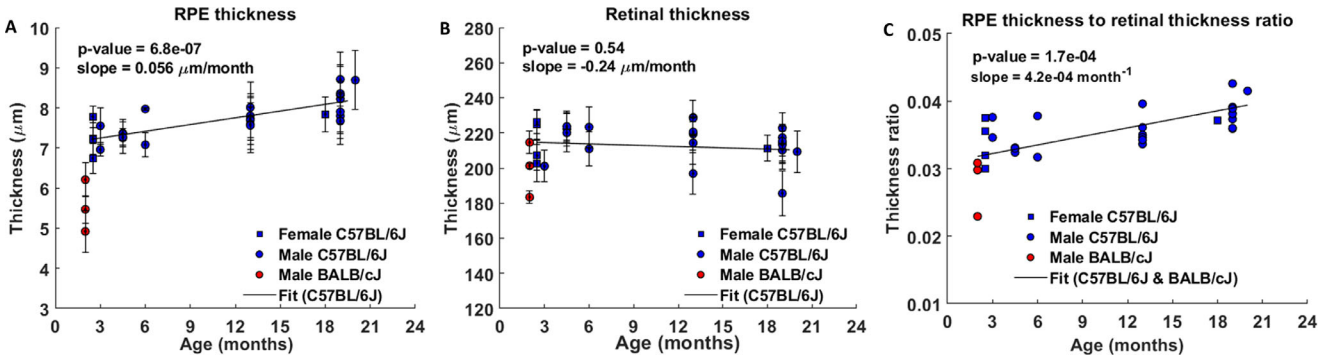

Figure 6. Linear mixed-effects models applied to cohort for (**A**) RPE thickness measured by method 2 (manually drawn BM to the outer OST boundary; see also Fig. 5); (**B**) retinal thickness; and (**C**) ratio of RPE thickness (method 2) to retinal thickness. *Error bars* are standard deviations in OCT measurements across locations.

extends the ideas of Jonnal et al.[16] to IS length dispersion in rods; specifically, we show that rod IS length dispersion, quantified directly with EM, explains band 2 thickness in mice.

Several alternative sources of band 2 reflectivity were also considered. Mitochondria were found as close as 5 µm to the ELM, consistent with prior mouse EM studies,[62] and were distributed throughout the ellipsoid of the IS,

Investigative Ophthalmology & Visual Science

inner to the IS/OS junction. Cone IS/OS junctions were not explicitly marked but were generally found between 10 and 13 µm from the ELM, also consistent with prior work.[73] Although mitochondria and cone IS/OS junctions clearly cannot explain the bulk of the band 2 reflectivity profile, which peaks around 20 µm from the ELM, they may indeed explain some of the reflectivity at the inner edge of band 2.

Study 3

RPE organelles may change in retinal diseases such as AMD, retinitis pigmentosa, and Stargardt's disease[74] but cannot yet be deciphered from OCT. We found that the OCT intensity from the hyperreflective RPE band within band 4 roughly followed the distribution of ED organelles (melanosomes and melanolipofuscin). In particular, reflectivity was higher in the apical RPE soma and processes where ED organelle density is highest and lower in the basal RPE where there are no ED organelles. This observation has two possible explanations, which are not mutually exclusive. First, the ED organelles may attenuate the OCT signal from more distal structures. Second, ED organelles may have a higher intrinsic backscattering. The first explanation implies that the derivative of the log intensity profile should follow the ED organelle density, and the second explanation implies that the intensity profile itself should follow the ED organelle density. Regardless of the explanation, we conclude that the RPE signal is dominated by melanosomes and melanolipofuscin in the apical RPE, rather than mitochondria and nuclei, which are located in the basal RPE (Supplementary Fig. S6). This finding is biophysically reasonable, given the high density of melanosomes, their wavelength-scale size, and the high refractive index of melanin relative to the cytoplasm.[75] The low RPE reflectivity in the young albino mouse (Fig. 5B) supports that melanin-containing melanosomes are the major RPE reflectivity sources, although we cannot exclude other genetic differences among strains. A preponderance of melanosome scattering was previously inferred in the RPE of the young adult human macula.[15] The present study strengthens these earlier findings by directly comparing organelle distributions and reflectivity profiles in the same subjects. Finally, as shown in Figure 4H, we observed that RPE thickness from OCT using method 2 (i.e., the distance from the BM peak to the dip outer to the OST) exceeded RPE thickness from EM (i.e., the distance from BM to the dip in ED organelle density between the RPE soma and the apical processes). This observation could be consistent with shrinkage of the RPE in EM sections. Assuming our BM reference surface is correct, this RPE thickness measurement includes the basal infoldings (Supplementary Fig. S6E). Having established that visible-light OCT affords the unique capability of measuring RPE thickness in vivo, we found that the RPE cells thicken with age in vivo in pigmented eyes (Fig. 6). This result is consistent with prior studies in rats[71] and humans.[76]

Study Limitations

As with any correlative study that bridges in vivo and ex vivo imaging, this work had numerous technical limitations:

1. Tissue distortion—Morphometric comparisons are challenging due to nonlinear tissue shrinkage, which means that the in vivo layer thicknesses are distorted to different degrees by histological processing. When the ILM and BM were aligned on OCT and histology, we found that the inner plexiform layer, ganglion cell layer, and nerve fiber layer complex appeared thicker on histology than in OCT, and the ONL seemed thinner on histology than OCT (Fig. 1), consistent with previous findings in the mouse.[23,77] We acknowledge that similar distortions caused by tissue dehydration in ex vivo EM could affect the outer retinal layers that were the subject of this study. This issue is further complicated by the fact that the hydration state and backscattering of the retina in vivo are known to change depending on the light adaptation state. The literature suggests that activity-dependent hydration is mostly confined to the outer segments and RPE.[78–80] Thus, these phenomena are likely to affect study 3 the most and may account for the lack of agreement in RPE thickness between OCT and EM. The literature also suggests that the IS length of study 2 was minimally affected by activity-dependent hydration,[78,79] although we cannot exclude such artifacts. We refrained from analyzing the outer segments or their relationship to the RPE, as they are particularly prone to distortion (Supplementary Fig. S6). For this same reason, we did not use the total photoreceptor length to perform normalized comparisons.
2. Oblique EM slices—The transmission electron microscope used in this study provided two-dimensional slices, not volumetric reconstructions; thus, oblique slicing may lead to overestimation of distances. To guard against this, we counted the rows of cell nuclei present in the ONL and found 11 or 12 cells (Fig. 1), as expected.[23] In the future, a block face scanning technique[81] would provide even more accurate distances. Additionally, organelles presented differing cross-sections depending on how they intersected the slice that was imaged by EM. Here, again, a block face technique[81] would enable more specific identification of organelles based on volumetric morphology.
3. Errors in the reference surfaces—Our reference surfaces may be incorrect. An incorrect reference surface would bias quantitative comparisons, leading to incorrect conclusions. For this reason, we attempted to choose well-accepted reference surfaces of the ELM and BM.[17,57]
4. Retinal stimulation in visible-light OCT—Visible-light–induced scattering changes seen in optophysiology,[82] along with outer segment and RPE swelling related to hydration,[78–80] are likely to be present in our study. We attempted to minimize these effects by aligning subjects under red light, but bleaching during imaging is unavoidable.
5. Refractive index assumptions—The error in refractive index is expected due to differences between the refractive index assumed during image reconstruction and the local tissue refractive index. A uniform water refractive index was assumed in this study. This assumption would tend to overestimate OCT dimensions, as water has a lower refractive index than biological tissues, and may lead to layer-dependent tissue distortions if different layers have different refractive indices.
6. Subject pool—Only four subjects were included in the EM comparative study. Nevertheless, the EM comparison required manual annotations of thousands of

Investigative Ophthalmology & Visual Science

organelles, and findings were highly consistent across all subjects. Finally, although this study afforded in vivo imaging and ex vivo histology in the same subjects, it was performed in mice; thus, results may not directly generalize to the human retina.

In spite of its limitations, this study showed that visible-light OCT can detect reflectivity patterns arising from micrometer-scale subcellular organization. These results provide a scientific rationale for continuing to improve the axial resolution of OCT.

Acknowledgments

Supported by grants from the National Institutes of Health (NS094681, EB029747, EY015387, EY031469, and EY012576) and Research to Prevent Blindness.

Disclosure: **P. Chauhan**, None; **A.M. Kho**, None; **P. FitzGerald**, None; **B. Shibata**, None; **V.J. Srinivasan**, Optovue (F)

References

1. Huang D, Swanson EA, Lin CP, et al. Optical coherence tomography. *Science*. 1991;254:1178–1181.
2. Swanson EA, Izatt JA, Hee MR, et al. In vivo retinal imaging by optical coherence tomography. *Opt Lett*. 1993;18:1864–1866.
3. de Sisternes L, Simon N, Tibshirani R, Leng T, Rubin DL. Quantitative SD-OCT imaging biomarkers as indicators of age-related macular degeneration progression. *Invest Ophthalmol Vis Sci*. 2014;55:7093–7103.
4. Fleckenstein M, Issa PC, Helb H-M, et al. High-resolution spectral domain-OCT imaging in geographic atrophy associated with age-related macular degeneration. *Invest Ophthalmol Vis Sci*. 2008;49:4137–4144.
5. Jung JJ, Chen CY, Mrejen S, et al. The incidence of neovascular subtypes in newly diagnosed neovascular age-related macular degeneration. *Am J Ophthalmol*. 2014;158:769–779.e2.
6. Manjunath V, Goren J, Fujimoto JG, Duker JS. Analysis of choroidal thickness in age-related macular degeneration using spectral-domain optical coherence tomography. *Am J Ophthalmol*. 2011;152:663–668.
7. Venhuizen FG, van Ginneken B, van Asten F, et al. Automated staging of age-related macular degeneration using optical coherence tomography. *Invest Ophthalmol Vis Sci*. 2017;58:2318–2328.
8. Chalam KV, Bressler SB, Edwards AR, et al. Retinal thickness in people with diabetes and minimal or no diabetic retinopathy: Heidelberg Spectralis optical coherence tomography. *Invest Ophthalmol Vis Sci*. 2012;53:8154–8161.
9. de Barros Garcia JMB, Isaac DLC, Avila M. Diabetic retinopathy and OCT angiography: clinical findings and future perspectives. *Int J Retina Vitreous*. 2017;3:14.
10. Jeoung JW, Choi YJ, Park KH, Kim DM. Macular ganglion cell imaging study: glaucoma diagnostic accuracy of spectral-domain optical coherence tomography. *Invest Ophthalmol Vis Sci*. 2013;54:4422–4429.
11. Takayama K, Hangai M, Durbin M, et al. A novel method to detect local ganglion cell loss in early glaucoma using spectral-domain optical coherence tomography. *Invest Ophthalmol Vis Sci*. 2012;53:6904–6913.
12. Fang L, Cunefare D, Wang C, Guymer RH, Li S, Farsiu S. Automatic segmentation of nine retinal layer boundaries in OCT images of non-exudative AMD patients using deep learning and graph search. *Biomed Opt Express*. 2017;8:2732–2744.
13. Sakamoto A, Hangai M, Yoshimura N. Spectral-domain optical coherence tomography with multiple B-scan averaging for enhanced imaging of retinal diseases. *Ophthalmology*. 2008;115:1071–1078.e7.
14. Kho AM, Zhang T, Zhu J, Merkle CW, Srinivasan VJ. Incoherent excess noise spectrally encodes broadband light sources. *Light Sci Appl*. 2020;9:172.
15. Zhang T, Kho AM, Yiu G, Srinivasan VJ. Visible light optical coherence tomography (OCT) quantifies subcellular contributions to outer retinal band 4. *Transl Vis Sci Technol*. 2021;10:30.
16. Jonnal RS, Kocaoglu OP, Zawadzki RJ, Lee S-H, Werner JS, Miller DT. The cellular origins of the outer retinal bands in optical coherence tomography images. *Invest Ophthalmol Vis Sci*. 2014;55:7904–7918.
17. Spaide RF, Curcio CA. Anatomical correlates to the bands seen in the outer retina by optical coherence tomography: literature review and model. *Retina*. 2011;31:1609.
18. Cuenca N, Ortuño-Lizarán I, Pinilla I. Cellular characterization of OCT and outer retinal bands using specific immunohistochemistry markers and clinical implications. *Ophthalmology*. 2018;125:407–422.
19. Curcio CA, Sparrow JR, Bonilha VL, Pollreisz A, Lujan BJ. Re: Cuenca et al.: cellular characterization of OCT and outer retinal bands using specific immunohistochemistry markers and clinical implications (Ophthalmology. 2018;125;407-422). *Ophthalmology*. 2018;125:e47–e48.
20. Toth CA, Narayan DG, Boppart SA, et al. A comparison of retinal morphology viewed by optical coherence tomography and by light microscopy. *Arch Ophthalmol*. 1997;115:1425–1428.
21. Berger A, Cavallero S, Dominguez E, et al. Spectral-domain optical coherence tomography of the rodent eye: highlighting layers of the outer retina using signal averaging and comparison with histology. *PLoS One*. 2014;9:e96494.
22. Ferguson LR, Grover S, Dominguez JM, Balaiya S, Chalam KV. Retinal thickness measurement obtained with spectral domain optical coherence tomography assisted optical biopsy accurately correlates with ex vivo histology. *PLoS One*. 2014;9:e111203.
23. Fischer MD, Huber G, Beck SC, et al. Noninvasive, in vivo assessment of mouse retinal structure using optical coherence tomography. *PLoS One*. 2009;4:e7507.
24. Kim KH, Puoris'haag M, Maguluri GN, et al. Monitoring mouse retinal degeneration with high-resolution spectral-domain optical coherence tomography. *J Vis*. 2008;8:17, 1–11.
25. Knott EJ, Sheets KG, Zhou Y, Gordon WC, Bazan NG. Spatial correlation of mouse photoreceptor-RPE thickness between SD-OCT and histology. *Exp Eye Res*. 2011;92:155–160.
26. Ryals RC, Andrews MD, Datta S, et al. Long-term characterization of retinal degeneration in Royal College of Surgeons rats using spectral-domain optical coherence tomography. *Invest Ophthalmol Vis Sci*. 2017;58:1378–1386.
27. Ferdous S, Liao KL, Gefke ID, et al. Age-related retinal changes in wild-type C57BL/6J mice between 2 and 32 months. *Invest Ophthalmol Vis Sci*. 2021;62:9.
28. Meleppat RK, Ronning KE, Karlen SJ, Burns ME, Pugh EN, Zawadzki RJ. In vivo multimodal retinal imaging of disease-related pigmentary changes in retinal pigment epithelium. *Sci Rep*. 2021;11:16252.
29. Beckmann L, Cai Z, Cole J, et al. In vivo imaging of the inner retinal layer structure in mice after eye-opening using visible-light optical coherence tomography. *Exp Eye Res*. 2021;211:108756.
30. Groh J, Stadler D, Buttmann M, Martini R. Non-invasive assessment of retinal alterations in mouse models of infantile and juvenile neuronal ceroid lipofuscinosis by spectral

domain optical coherence tomography. *Acta Neuropathol Commun*. 2014;2:54.
31. Xie W, Zhao M, Tsai S-H, et al. Correlation of spectral domain optical coherence tomography with histology and electron microscopy in the porcine retina. *Exp Eye Res*. 2018;177:181–190.
32. Litts KM, Zhang Y, Freund KB, Curcio CA. Optical coherence tomography and histology of age-related macular degeneration support mitochondria as reflectivity sources. *Retina*. 2018;38:445–461.
33. Anger EM, Unterhuber A, Hermann B, et al. Ultrahigh resolution optical coherence tomography of the monkey fovea. Identification of retinal sublayers by correlation with semithin histology sections. *Exp Eye Res*. 2004;78:1117–1125.
34. Gloesmann M, Hermann B, Schubert C, Sattmann H, Ahnelt PK, Drexler W. Histologic correlation of pig retina radial stratification with ultrahigh-resolution optical coherence tomography. *Invest Ophthalmol Vis Sci*. 2003;44:1696–1703.
35. Spaide RF. Outer retinal bands. *Invest Ophthalmol Vis Sci*. 2015;56:2505–2506.
36. Pollreisz A, Neschi M, Sloan KR, et al. Atlas of human retinal pigment epithelium organelles significant for clinical imaging. *Invest Ophthalmol Vis Sci*. 2020;61:13.
37. Menghini M, Lujan BJ, Zayit-Soudry S, et al. Correlation of outer nuclear layer thickness with cone density values in patients with retinitis pigmentosa and healthy subjects. *Invest Ophthalmol Vis Sci*. 2015;56:372–381.
38. Wu Z, Ayton LN, Guymer RH, Luu CD. Second reflective band intensity in age-related macular degeneration. *Ophthalmology*. 2013;120:1307–1308.e1.
39. Wu Z, Ayton LN, Guymer RH, Luu CD. Relationship between the second reflective band on optical coherence tomography and multifocal electroretinography in age-related macular degeneration. *Invest Ophthalmol Vis Sci*. 2013;54:2800–2806.
40. Sundaram V, Wilde C, Aboshiha J, et al. Retinal structure and function in achromatopsia: implications for gene therapy. *Ophthalmology*. 2014;121:234–245.
41. Oishi A, Shimozono M, Mandai M, Hata M, Nishida A, Kurimoto Y. Recovery of photoreceptor outer segments after anti-VEGF therapy for age-related macular degeneration. *Graefes Arch Clin Exp Ophthalmol*. 2013;251:435–440.
42. Yao X, Son T, Kim T-H, Le D. Interpretation of anatomic correlates of outer retinal bands in optical coherence tomography. *Exp Biol Med*. 2021;246:2140–2150.
43. Aizawa S, Mitamura Y, Baba T, Hagiwara A, Ogata K, Yamamoto S. Correlation between visual function and photoreceptor inner/outer segment junction in patients with retinitis pigmentosa. *Eye (Lond)*. 2009;23:304–308.
44. Baba T, Yamamoto S, Arai M, et al. Correlation of visual recovery and presence of photoreceptor inner/outer segment junction in optical coherence images after successful macular hole repair. *Retina*. 2008;28:453–458.
45. Mitamura Y, Aizawa S, Baba T, Hagiwara A, Yamamoto S. Correlation between retinal sensitivity and photoreceptor inner/outer segment junction in patients with retinitis pigmentosa. *Br J Ophthalmol*. 2009;93:126–127.
46. Ota M, Tsujikawa A, Murakami T, et al. Foveal photoreceptor layer in eyes with persistent cystoid macular edema associated with branch retinal vein occlusion. *Am J Ophthalmol*. 2008;145:273–280.e1.
47. Spaide RF, Koizumi H, Freund KB. Photoreceptor outer segment abnormalities as a cause of blind spot enlargement in acute zonal occult outer retinopathy–complex diseases. *Am J Ophthalmol*. 2008;146:111–120.
48. Landa G, Su E, Garcia PM, Seiple WH, Rosen RB. Inner segment–outer segment junctional layer integrity and corresponding retinal sensitivity in dry and wet forms of age-related macular degeneration. *Retina*. 2011;31:364–370.
49. Fujita K, Shinoda K, Imamura Y, et al. Correlation of integrity of cone outer segment tips line with retinal sensitivity after half-dose photodynamic therapy for chronic central serous chorioretinopathy. *Am J Ophthalmol*. 2012;154:579–585.
50. Lau T, Wong IY, Iu L, et al. En-face optical coherence tomography in the diagnosis and management of age-related macular degeneration and polypoidal choroidal vasculopathy. *Indian J Ophthalmol*. 2015;63:378–383.
51. Tortorella P, D'Ambrosio E, Iannetti L, De Marco F, La Cava M. Correlation between visual acuity, inner segment/outer segment junction, and cone outer segment tips line integrity in uveitic macular edema. *Biomed Res Int*. 2015;2015:853728.
52. Lee KE, Heitkotter H, Carroll J. Challenges associated with ellipsoid zone intensity measurements using optical coherence tomography. *Transl Vis Sci Technol*. 2021;10:27.
53. Fernández EJ, Hermann B, Považay B, et al. Ultrahigh resolution optical coherence tomography and pancorrection for cellular imaging of the living human retina. *Opt Express*. 2008;16:11083–11094.
54. Lu R-W, Zhang Q-X, Yao X, et al. Investigation of the hyper-reflective inner/outer segment band in optical coherence tomography of living frog retina. *J Biomed Opt*. 2012;17:060504.
55. Volland S, Esteve-Rudd J, Hoo J, Yee C, Williams DS. A comparison of some organizational characteristics of the mouse central retina and the human macula. *PLoS One*. 2015;10:e0125631.
56. Boulton M, Dayhaw-Barker P. The role of the retinal pigment epithelium: topographical variation and ageing changes. *Eye (Lond)*. 2001;15:384–389.
57. Staurenghi G, Sadda S, Chakravarthy U, Spaide RF. Proposed lexicon for anatomic landmarks in normal posterior segment spectral-domain optical coherence tomography: the IN•OCT consensus. *Ophthalmology*. 2014;121:1572–1578.
58. Jeon CJ, Strettoi E, Masland RH. The major cell populations of the mouse retina. *J Neurosci*. 1998;18:8936–8946.
59. Carter-Dawson LD, Lavail MM. Rods and cones in the mouse retina. I. Structural analysis using light and electron microscopy. *J Comp Neurol*. 1979;188:245–262.
60. Lee W, Noupuu K, Oll M, et al. The external limiting membrane in early-onset Stargardt disease. *Invest Ophthalmol Vis Sci*. 2014;55:6139–6149.
61. Cuenca N, Ortuño-Lizarán I, Sánchez-Sáez X, et al. Interpretation of OCT and OCTA images from a histological approach: clinical and experimental implications. *Prog Retin Eye Res*. 2020;77:100828.
62. Kam JH, Jeffery G. To unite or divide: mitochondrial dynamics in the murine outer retina that preceded age related photoreceptor loss. *Oncotarget*. 2015;6:26690.
63. Berman ER. *Biochemistry of the Eye*. New York: Springer; 1991:201–290.
64. Baumann B, Baumann SO, Konegger T, et al. Polarization sensitive optical coherence tomography of melanin provides intrinsic contrast based on depolarization. *Biomed Opt Express*. 2012;3:1670–1683.
65. Song W, Zhang L, Ness S, Yi J. Wavelength-dependent optical properties of melanosomes in retinal pigmented epithelium and their changes with melanin bleaching: a numerical study. *Biomed Opt Express*. 2017;8:3966–3980.
66. Yiu G, Vuong VS, Oltjen S, et al. Effect of uveal melanocytes on choroidal morphology in rhesus macaques and humans on enhanced-depth imaging optical coherence tomography. *Invest Ophthalmol Vis Sci*. 2016;57:5764–5771.

Investigative Ophthalmology & Visual Science

67. Zhang Q-X, Lu R-W, Messinger JD, Curcio CA, Guarcello V, Yao X-C. In vivo optical coherence tomography of light-driven melanosome translocation in retinal pigment epithelium. *Sci Rep*. 2013;3:2644.
68. Zhang T, Kho AM, Zawadzki RJ, Jonnal RS, Yiu G, Srinivasan VJ. Visible light OCT improves imaging through a highly scattering retinal pigment epithelial wall. *Opt Lett*. 2020;45:5945–5948.
69. Yi J, Chen S, Shu X, Fawzi AA, Zhang HF. Human retinal imaging using visible-light optical coherence tomography guided by scanning laser ophthalmoscopy. *Biomed Opt Express*. 2015;6:3701–3713.
70. Chai Z, Silverman D, Li G, Williams D, Raviola E, Yau K-W. Light-dependent photoreceptor orientation in mouse retina. *Sci Adv*. 2020;6:eabe2782.
71. Katz ML, Robison WG. Age-related changes in the retinal pigment epithelium of pigmented rats. *Exp Eye Res*. 1984;38:137–151.
72. Chandler M, Smith P, Samuelson D, MacKay E. Photoreceptor density of the domestic pig retina. *Vet Ophthalmol*. 1999;2:179–184.
73. Fu Y, Yau K-W. Phototransduction in mouse rods and cones. *Pflügers Arch*. 2007;454:805–819.
74. Dartt DA. *Encyclopedia of the Eye*. Cambridge, MA: Academic Press; 2010.
75. Song W, Zhang L, Ness S, Yi J. Wavelength-dependent optical properties of melanosomes in retinal pigmented epithelium and their changes with melanin bleaching: a numerical study. *Biomed Opt Express*. 2017;8:3966–3980.
76. Weiter J, Delori F, Wing G, Fitch K. Retinal pigment epithelial lipofuscin and melanin and choroidal melanin in human eyes. *Invest Ophthalmol Vis Sci*. 1986;27:145–152.
77. Cuenca N, Fernández-Sánchez L, Sauvé Y, et al. Correlation between SD-OCT, immunocytochemistry and functional findings in an animal model of retinal degeneration. *Front Neuroanat*. 2014;8:151.
78. Berkowitz BA, Podolsky RH, Qian H, et al. Mitochondrial respiration in outer retina contributes to light-evoked increase in hydration in vivo. *Invest Ophthalmol Vis Sci*. 2018;59:5957–5964.
79. Kim T-H, Ding J, Yao X. Intrinsic signal optoretinography of dark adaptation kinetics. *Sci Rep*. 2022;12:2475.
80. Messner A, Aranha dos Santos V, Stegmann H, et al. Quantification of intrinsic optical signals in the outer human retina using optical coherence tomography. *Ann N Y Acad Sci*. 2022;1510:145–157.
81. Pollreisz A, Messinger JD, Sloan KR, et al. Visualizing melanosomes, lipofuscin, and melanolipofuscin in human retinal pigment epithelium using serial block face scanning electron microscopy. *Exp Eye Res*. 2018;166:131–139.
82. Zhang P, Zawadzki RJ, Goswami M, et al. In vivo optophysiology reveals that G-protein activation triggers osmotic swelling and increased light scattering of rod photoreceptors. *Proc Natl Acad Sci USA*. 2017;114:E2937–E2946.